Worst-Case Scenarios of Radiated-Susceptibility Effects in a Multiport System Subject to Intentional Electromagnetic Interference

TAO LIANG[ID]**, GIORDANO SPADACINI**[ID]**, (Senior Member, IEEE),**
FLAVIA GRASSI[ID]**, (Senior Member, IEEE), AND**
SERGIO AMEDEO PIGNARI[ID]**, (Fellow, IEEE)**
Dipartimento di Elettronica Informazione e Bioingegneria, Politecnico di Milano, 20133 Milan, Italy

Corresponding author: Giordano Spadacini (giordano.spadacini@polimi.it)

ABSTRACT This paper presents a method to assess intentional electromagnetic interference (IEMI) in a linear multiport system, due to coupling with a high-power electromagnetic (HPEM) field. First, an approach based on the Lorentz reciprocity theorem is proposed to model field coupling for the arbitrary direction of incidence and polarization, which minimizes the number of required full-wave numerical simulations. Afterward, three constrained-optimization problems are identified to describe the worst-case scenarios related to different radiated-susceptibility effects at the system's ports. Namely, under the assumption of limited bandwidth and finite energy density, the spectrum and the waveform of the HPEM field are found so to maximize the dissipated energy, the peak, and the rectified impulse of the induced voltage waveform. It is shown analytically that in the worst-case energy scenario, the HPEM field shall be a properly tuned narrowband field, whereas in the worst-case voltage peak scenario a wideband field properly matched to the frequency response of the system is needed. In addition, it is shown that the rectified impulse of the induced voltage can be made arbitrarily large by reducing the impinging field bandwidth. A typical printed-circuit board interconnect for low-voltage differential signaling is used to exemplify and validate the proposed approach. Furthermore, uncertainty-quantification techniques are exploited to cope with the lack of knowledge about the incidence and polarization parameters of the HPEM field, as well as to account for uncertain geometrical parameters of the victim system.

INDEX TERMS High-power electromagnetics (HPEM), intentional electromagnetic interference (IEMI), low-voltage differential signaling (LVDS), radiated susceptibility.

I. INTRODUCTION

The advent of enabling technologies like 5G Communication and Artificial Intelligence, as well as revolutionary concepts like the Internet of Things, Smart Cities, and Industry 4.0 are pushing modern society towards an unprecedent dependence upon electronics. In this context, the protection of circuits and systems against Intentional Electromagnetic Interference (IEMI) is gaining increasing interest from engineers and researchers [1]–[3]. According to standard IEC-61000-2-13, IEMI exploits "intentional malicious generation of electromagnetic energy, introducing noise or signals into electric and

electronic systems, thus disrupting, confusing or damaging these systems, for terrorist or criminal purposes" [4].

IEMI attacks based on the generation of radiated electromagnetic fields are made possible by High-Power Electromagnetic (HPEM) technology, a discipline subject to extensive research in past years [5]. The term HPEM was initially used to describe accidental electromagnetic environments where peak values of the electric field reach and exceed hundreds of V/m, generated by phenomena like lightning strikes and high-altitude nuclear bursts [6]. The development of high-power microwave (HPM) sources and impulse radiating antennas (IRAs) [7] paved the way to the intentional generation of transient HPEM fields with either narrowband or wideband spectral content, specifically targeted to IEMI purposes [6].

The associate editor coordinating the review of this manuscript and approving it for publication was Mohamed Kheir.

Several studies were carried out to investigate such HPEM environments [8] and to assess the susceptibility levels of specific devices and systems through extensive experimental campaigns [9]–[13]. From the viewpoint of modeling and simulation, assessing potential IEMI effects remains a challenging task, because of lack of knowledge about all possible disrupting HPEM environments, which can be the most various and unpredictable.

For instance, intentional HPEM fields may encompass both narrowband HPM waveforms having any center frequency in the GHz range, and ultra-wideband waveforms characterized by any spectral content (not standardized) typically above 300 MHz [4]. In this connection, the investigation of worst-case scenarios is a reasonable solution, that is, considering the HPEM field waveform which leads to the maximization of significant figures of merit correlated to susceptibility mechanisms. A second source of uncertainty in the prediction of radiated IEMI effects is the lack of knowledge about the direction of incidence and polarization of the plane-wave electromagnetic field impinging onto the victim system (in the far-field region of the IRA). In this case, statistical techniques can be used to define suitable input random variables (RVs) and characterize the output quantities of interest through distribution functions and statistical estimates [14].

In line with this approach, a combined worst-case/statistical method to model IEMI effects was proposed in [15]. The maximum peak in the waveform of the voltage induced across an electric port of the system was considered as the significant figure of merit for susceptibility assessment. Under the assumptions of limited bandwidth and finite energy density of the HPEM field, the electric-field waveform leading to the maximization of the voltage peak was derived by solving a constrained-optimization problem. Finally, the cumulative distribution function (cdf) of the worst-case voltage peak was characterized by Monte Carlo (MC) simulations, to account for random incidence and polarization angles of the plane-wave field. The rationale of [15] was later exploited in [16]–[20] to analyze in depth the properties of a specific system, namely, common-mode (CM) interference induced in a wiring harness running above ground [16].

This paper presents a more general method for IEMI assessment, which includes the previous findings in [15] as a particular case. First, the analysis is extended to a victim system having multiple electric ports. Second, it is recognized that other figures of merits beside the instantaneous peak are usually considered in radiated-susceptibility studies [12], [21]–[23]. In particular, integral quantities called *p*-norms can be generally defined as

$$\| s(x) \|_p = \left[\int_{-\infty}^{+\infty} |s(x)|^p \, dx \right]^{1/p} \qquad (1)$$

where $s(x)$ is a signal in either frequency domain or time domain according to the applicative framework [24]. Specifically, the three quantities of interest in this paper are a) the 1-norm of the induced voltage, called rectified impulse, related to stress mechanisms in dielectrics; b) the squared

TABLE 1. Figures of merit for potential susceptibility effects.

Norm	Expression	Waveform Attribute	Susceptibility Mechanisms
∞-norm	$\max\{|v(t)|\}$	peak	bit error/ analogue error/ overvoltage breakdown
squared 2-norm	$\int_{-\infty}^{+\infty} |v(t)|^2 \, dt$	energy	overheat/burnout
1-norm	$\int_{-\infty}^{+\infty} |v(t)| \, dt$	rectified impulse	dielectric puncture

2-norm of the voltage, related to energy dissipation in conductive media; and c) the ∞-norm, which turns out to be equivalent to the voltage peak considered in [15] by virtue of its mathematical properties [24]. These figures of merit and their relevant susceptibility effects are summarized in Table 1 [13], [21], [25]. Lastly, the statistics of these figures of merit is investigated not only with respect to random incidence and polarization of the HPEM field as in [15], but also in case of geometrical parameters affected by uncertainty. To this aim, a stochastic reduced order model (SROM) combined with the MC method is proposed to reduce the computational burden.

The paper is organized as follows. Section II introduces a computational scheme to model coupling of a plane-wave field to a multiport victim system, based on the Lorentz reciprocity theorem of electromagnetics. The use of reciprocity allows evaluating the transfer ratios (called *coupling lengths*) between the voltage induced across port loads and the incident field to be determined for arbitrary direction of incidence and polarization, through a minimum number of numerical full-wave simulations. Section III defines and solves three constrained-optimization problems aimed at maximizing the dissipated energy, the peak, and the rectified impulse of the induced voltage, seen as different worst-case scenarios for radiated susceptibility effects. Solutions are obtained in closed form and unveil significant properties about the spectral content (narrowband, wideband) of the worst-case HPEM field. Section IV exemplifies the proposed method and validates the worst-case scenarios with reference to a printed-circuit board (PCB) interconnect for low-voltage differential signaling (LVDS). Additionally, the cdfs of the worst-case peak and dissipated energy are exemplified. Finally, conclusions are drawn in Section V.

II. RECIPROCITY-BASED APPROACH FOR MODELING FIELD COUPLING TO A MULTIPORT SYSTEM

A reciprocity-based computational method is proposed to predict the voltage induced across target loads in any victim system illuminated by an HPEM field. In this respect, two broad, underlying assumptions are: a) the system can be modeled as a multiport network with accessible electric ports, where voltage and current can be consistently defined according to circuit theory [26]; b) the system is linear, thus allowing the application of the Lorentz reciprocity theorem [27], as well as the Fourier transformation for
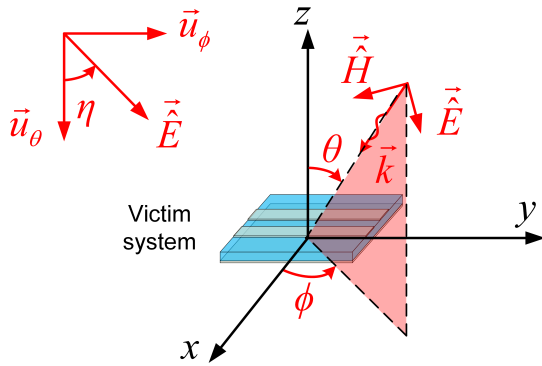
FIGURE 1. Linearly polarized plane-wave electromagnetic field impinging on a victim system (e.g., a PCB).

FIGURE 2. Representation of the victim system as a multiport network.

frequency-domain analysis. A modifier caret (^) and an arrow (→) above symbols are hereafter used to indicate phasor and vector quantities, respectively.

In Fig. 1, the HPEM field is modeled as a linearly polarized plane-wave, impinging a victim system positioned in the origin of spherical coordinates (r, θ, ϕ) associated with unit vectors $\vec{u}_r$, $\vec{u}_\theta$, $\vec{u}_\phi$. The wave vector is $\vec{k} = -k\,\vec{u}_r$, where $k = \omega/c_0$ is the wave number, ω is the angular frequency, $c_0 = 1/\sqrt{\varepsilon_0\mu_0}$ is the speed of light in free space, μ_0 and ε_0 are the magnetic permeability and electric permittivity of vacuum, respectively. The direction of $\vec{k}$ is defined by polar angle θ and azimuth angle ϕ. The incident electric field $\hat{E}_i$ lies in the plane perpendicular to $\vec{k}$ and can be decomposed into orthogonal vector components as

$$\vec{E}_i = \hat{E}_i\,(\omega)\left(\cos\eta \cdot \vec{u}_\theta + \sin\eta \cdot \vec{u}_\phi\right) \qquad (2)$$

where η is the polarization angle.

For the evaluation of voltages induced in the system ports by the above incident field, the proposed approach initially entails a change of perspective. Namely, it considers a different (i.e., reciprocal) problem where the system is treated in transmitting mode as an unintentional radiator and the objective is to compute its input-impedance and far-field radiation pattern.

A. RECIPROCAL TRANSMITTING-MODE PROBLEM
The multiport structure of the victim system is represented in Fig. 2, where $\hat{I}_{P,n}$ and $\hat{V}_{P,n}$, $n = 1, 2, \ldots, N$ are N port currents and voltages, respectively. By introducing column vectors

$$\hat{\mathbf{V}}_{\mathbf{P}} = \left[\hat{V}_{P,1}, \hat{V}_{P,2}, \ldots, \hat{V}_{P,N}\right]^{\mathrm{T}} \qquad (3)$$

$$\hat{\mathbf{I}}_{\mathbf{P}} = \left[\hat{I}_{P,1}, \hat{I}_{P,2}, \ldots, \hat{I}_{P,N}\right]^{\mathrm{T}} \qquad (4)$$

where T denotes vector transposition, the frequency-dependent input-impedance matrix $\hat{\mathbf{Z}}_{\mathbf{a}}$ of the multiport network is defined by the current-controlled constitutive relationship

$$\hat{\mathbf{V}}_{\mathbf{P}} = \hat{\mathbf{Z}}_{\mathbf{a}}\hat{\mathbf{I}}_{\mathbf{P}} \qquad (5)$$
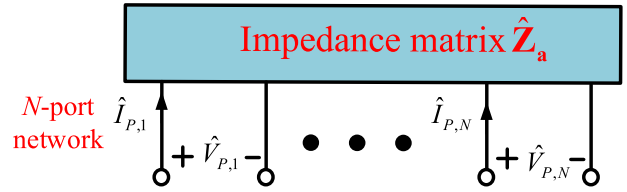
Additionally, by assuming that only the n-th port of the system is fed by an arbitrary current source $\hat{I}_{P,n}$, while the other ports are open-ended (i.e., $\hat{I}_{P,m} = 0$, $m \neq n$), the n-th decoupled and normalized radiation pattern is here suitably defined as

$$
\begin{aligned}
\vec{F}_n\,(\omega, \theta, \phi) &= re^{jkr}\vec{E}_{r,n}(\omega, r, \theta, \phi)\Big/\hat{I}_{P,n} \\
&= \hat{F}_{\theta,n}(\omega, \theta, \phi)\vec{u}_\theta + \hat{F}_{\phi,n}(\omega, \theta, \phi)\vec{u}_\phi
\end{aligned}
\qquad (6)
$$

where $\vec{E}_{r,n}(\omega, r, \theta, \phi)$ is the electric field of the plane-wave radiated in the far-field region [27]. Note that the result of (6) is both a complex and vector quantity, which is normalized to the feeding current (hence it is expressed in Ohm) and loses dependence on the radial coordinate. The radiation patterns pertaining to all the N ports can be collected in a column vector $\vec{\mathbf{F}} = \left[\vec{F}_1, \vec{F}_2, \ldots, \vec{F}_N\right]^{\mathrm{T}}$, and decomposed in orthogonal components:

$$\vec{\mathbf{F}} = \hat{\mathbf{F}}_{\boldsymbol{\theta}}\vec{u}_\theta + \hat{\mathbf{F}}_{\boldsymbol{\phi}}\vec{u}_\phi \qquad (7)$$

$$\hat{\mathbf{F}}_{\boldsymbol{\theta}} = \left[\hat{F}_{\theta,1}, \hat{F}_{\theta,2}, \ldots, \hat{F}_{\theta,N}\right]^{\mathrm{T}} \qquad (8)$$

$$\hat{\mathbf{F}}_{\boldsymbol{\phi}} = \left[\hat{F}_{\phi,1}, \hat{F}_{\phi,2}, \ldots, \hat{F}_{\phi,N}\right]^{\mathrm{T}} \qquad (9)$$

The evaluation of $\hat{\mathbf{Z}}_{\mathbf{a}}$ and $\vec{\mathbf{F}}$ in the bandwidth of interest is a key task of the proposed approach, which can be accomplished by using any full-wave numerical method for the solution of Maxwell's equations, e.g., Finite Integration Technique (FIT), Method of Moments (MoM), Finite Element Method (FEM), etc. The choice of the most suitable method is driven by the peculiar characteristics of the system under analysis, in terms of geometry, media, electrical dimensions.

It is worth nothing, however, that port feeding conditions commonly implemented in numerical solvers for radio-frequency and microwave applications do not usually match the previous current-controlled characterization. Generally, as shown in Fig. 3, one electric port at a time (e.g., port 1 in the figure) is excited by an arbitrary voltage source $\hat{V}_{S,n}$ with series impedance $\hat{Z}_{S,n}$, while the remaining ports are loaded by passive arbitrary impedances $\hat{Z}_{S,m}$, $m \neq n$. Indeed, these are the proper loading conditions when working with scattering (s-) parameters (in that framework, $\hat{Z}_{S,k}$ plays the role of reference impedance) [26]. Although the definition (5) retains validity and the impedance matrix $\hat{\mathbf{Z}}_{\mathbf{a}}$ can be easily retrieved from the simulation output (e.g., by processing the s-parameter matrix, [26]), the radiation pattern computed for
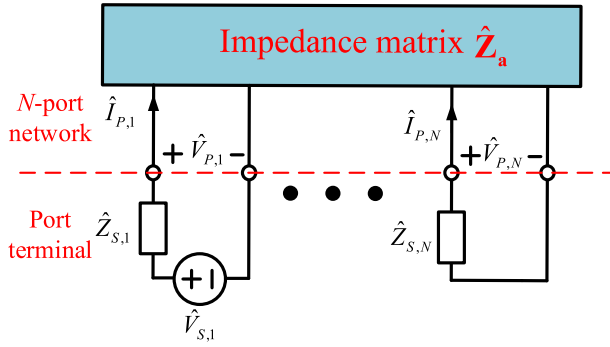
FIGURE 3. Loading conditions at the *N* ports of the victim system in a transmitting-mode problem. Without loss of generality, port 1 is excited and the remaining ports are connected to passive impedances.

FIGURE 4. Equivalent circuit of the victim system in receiving mode. Voltage sources in series at system ports account for external-field excitation. Port terminals are connected to load impedances.

loaded ports does not conform to the desired definition (6) of a decoupled, normalized radiation pattern, since all ports have non-null currents in general.

In particular, a number of N full-wave simulations (one for each single-port excitation) must be carried out to compute the radiation patterns $\vec{F}_{R,n}$, $n = 1, 2, \ldots, N$ defined as

$$\vec{F}_{R,n}(\omega, \theta, \phi) = r e^{jkr} \vec{E}_{r,n}(\omega, r, \theta, \phi) \quad (10)$$

which are eventually collected in a column vector $\vec{\mathbf{F}}_{\mathbf{R}} = \left[\vec{F}_{R,1}, \vec{F}_{R,2}, \ldots, \vec{F}_{R,N} \right]^{\mathrm{T}}$. To retrieve the decoupled and normalized radiation patterns (6), let $\hat{\mathbf{Z}}_{\mathbf{S}} = \mathrm{diag}\left\{ \hat{Z}_{S,1}, \hat{Z}_{S,2}, \ldots, \hat{Z}_{S,N} \right\}$ be the diagonal matrix of port impedances and let $\hat{\mathbf{V}}_{\mathbf{S},n} = \left[0, \ldots, \hat{V}_{S,n}, \ldots, 0 \right]^{\mathrm{T}}$ be the n-th column vector of voltage sources describing a single-port excitation experiment. By resorting to circuit theory, the vector of port currents for the n-th single-port excitation can be cast as

$$\hat{\mathbf{I}}_{\mathbf{P},n} = \left(\hat{\mathbf{Z}}_{\mathbf{a}} + \hat{\mathbf{Z}}_{\mathbf{S}} \right)^{-1} \hat{\mathbf{V}}_{\mathbf{S},n} \quad (11)$$

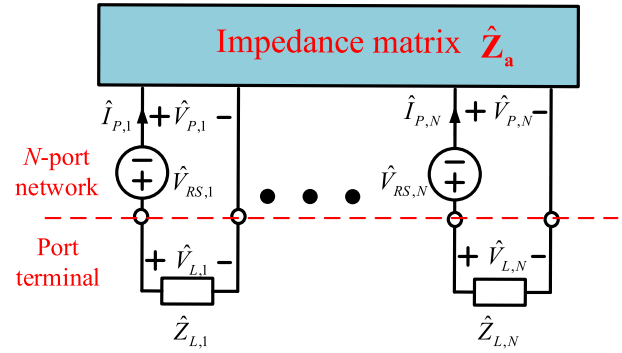Accordingly, the normalized and decoupled radiation patterns defined in (6) can be readily obtained by

$$\vec{\mathbf{F}} = \left[\hat{\mathbf{I}}_{\mathbf{PM}} \right]^{-1} \vec{\mathbf{F}}_{\mathbf{R}} \quad (12)$$

where the N-by-N matrix $\hat{\mathbf{I}}_{\mathbf{PM}} = \left[\hat{\mathbf{I}}_{\mathbf{P},1}^{\mathrm{T}}, \hat{\mathbf{I}}_{\mathbf{P},2}^{\mathrm{T}} \ldots; \hat{\mathbf{I}}_{\mathbf{P},N}^{\mathrm{T}} \right]$ collects the port-current vectors in (11).

B. RECEIVING-MODE PROBLEM

The evaluation of $\hat{\mathbf{Z}}_{\mathbf{a}}$ and $\vec{\mathbf{F}}$ carried out by N full-wave simulations in transmitting mode can be now exploited to solve the original receiving-mode problem by virtue of reciprocity.

The multiport system subject to external HPEM field illumination is represented in Fig. 4. According to the Lorentz reciprocity theorem formulated for antennas [28], this multiport network is described by the input-impedance matrix $\hat{\mathbf{Z}}_{\mathbf{a}}$ and series voltage sources $\hat{V}_{RS,n}$ at each port, accounting for coupling with the incident plane-wave electromagnetic field.

Specifically, the column vector of voltage sources $\hat{\mathbf{V}}_{\mathbf{RS}} = \left[\hat{V}_{RS,1}, \hat{V}_{RS,2}, \ldots, \hat{V}_{RS,N} \right]^{\mathrm{T}}$ can be cast as

$$\hat{\mathbf{V}}_{\mathbf{RS}} = -\frac{2j\lambda_0}{Z_0} \hat{E}_i \left[\hat{\mathbf{F}}_{\boldsymbol{\theta}} \cos \eta + \hat{\mathbf{F}}_{\boldsymbol{\phi}} \sin \eta \right] \quad (13)$$

where j is imaginary unit, $\lambda_0 = 2\pi c_0 / \omega$ and $Z_0 = \sqrt{\mu_0 / \varepsilon_0}$ are the free-space wavelength and wave impedance, respectively [15], [28].

Impedances $\hat{Z}_{L,i}$ in Fig. 4 represent the target loads of the victim system, for which the induced voltage $\hat{V}_{L,i}$ and current $\hat{I}_{L,i}$ can be evaluated by circuit theory as

$$\hat{\mathbf{I}}_{\mathbf{L}} = \left[\hat{I}_{L,1}, \hat{I}_{L,2}, \ldots, \hat{I}_{L,N} \right]^{\mathrm{T}} = -\left(\hat{\mathbf{Z}}_{\mathbf{a}} + \hat{\mathbf{Z}}_{\mathbf{L}} \right)^{-1} \hat{\mathbf{V}}_{\mathbf{RS}} \quad (14)$$

$$\hat{\mathbf{V}}_{\mathbf{L}} = \left[\hat{V}_{L,1}, \hat{V}_{L,2}, \ldots, \hat{V}_{L,N} \right]^{\mathrm{T}} = -\hat{\mathbf{Z}}_{\mathbf{L}} \hat{\mathbf{I}}_{\mathbf{L}} \quad (15)$$

where $\hat{\mathbf{Z}}_{\mathbf{L}} = \mathrm{diag}\left\{ \hat{Z}_{L,1}, \ldots, \hat{Z}_{L,i}, \ldots, \hat{Z}_{L,N} \right\}$.

Solution (14)-(15) is derived in the frequency domain, hence the input electric field $\hat{E}_i(\omega)$ and the output port voltages $\hat{\mathbf{V}}_{\mathbf{L}}(\omega)$ are concerned as spectrum densities. The Inverse Fourier Transform (IFT) is needed to express the corresponding time-domain waveforms.

For simplicity of notation, a frequency-domain transfer function called *coupling length* (dimensions in meters) is defined as

$$\hat{\mathbf{L}}(\omega) = \left[\hat{L}_1(\omega), \hat{L}_2(\omega), \ldots \hat{L}_N(\omega) \right]^{\mathrm{T}} = \frac{\hat{\mathbf{V}}_{\mathbf{L}}(\omega)}{\hat{E}_i(\omega)} \quad (16)$$

whose expression follows from (13)-(16) in the form

$$\hat{\mathbf{L}} = -\frac{2j\lambda_0}{Z_0} \hat{\mathbf{Z}}_{\mathbf{L}} \left(\hat{\mathbf{Z}}_{\mathbf{a}} + \hat{\mathbf{Z}}_{\mathbf{L}} \right)^{-1} \left[\hat{\mathbf{F}}_{\boldsymbol{\theta}} \cos \eta + \hat{\mathbf{F}}_{\boldsymbol{\phi}} \sin \eta \right] \quad (17)$$

Accordingly, the induced voltage across load $\hat{Z}_{L,n}$ at port n can be obtained by IFT as

$$V_{L,n}(t) = \frac{1}{2\pi} \int_{-\infty}^{+\infty} \hat{E}_i(\omega) \hat{L}_n(\omega) e^{j\omega t} d\omega \quad (18)$$

where t is time. Note that both $\hat{E}_i(\omega)$ and $\hat{L}_n(\omega)$ are bilateral spectra, and their negative-frequency components can

be constructed by enforcing conjugate symmetry, that is $\hat{E}_i(-\omega) = \hat{E}_i^*(\omega)$, $\hat{L}_n(-\omega) = \hat{L}_n^*(\omega)$, where the asterisk denotes complex conjugation.

It is worth noting that the proposed reciprocity-based approach extends to a N-port victim system from the single-port derivation in [15], while retaining the advantages in computational terms. Namely, only N full-wave simulations of the system (in transmitting mode) are required to evaluate $\vec{\hat{F}}$ and $\hat{\mathbf{Z}}_a$. These quantities can be stored in memory and subsequently post-processed by (13)-(18), enabling fast re-computation of the solution at any port, and for any possible incidence angles θ, ϕ and polarization angle η of the impinging plane-wave field in Fig. 1.

III. WORST-CASE IEMI SCENARIOS

In this section, the time-domain, reciprocity-based representation (18) of the induced voltage is exploited to investigate different worst-case scenarios. The objective is finding the electric-field spectrum $\hat{E}_i(\omega)$ and waveform $E_i(t)$ which maximize a specific norm of the voltage waveform $V_{L,n}(t)$ induced in a system port. Specifically, the maximum energy, peak value, and rectified impulse of the induced voltage are of interest.

In view of technological limitations of practical HPEM radiation systems [12], two assumptions are enforced for the impinging electric field: a) the energy density W_E (expressed in J/m^2) is finite; b) the signal is band-limited in the interval $[\omega_1, \omega_2]$. Given hypothesis a), only transient pulses tending to zero for $t \to \infty$ are of interest (i.e., steady-state sinusoidal signals of finite power are not considered). As a further clarification, for disruptors able to deliver a burst of repetitive pulses (with repetition period much longer than the duration of each single pulse), the proposed analysis can be referred to a single pulse. The second assumption b) removes the infinite integration extremes in (18) and can be interpreted, in practical terms, according to the bandwidth definition given in IEC 61000-2-13, namely, the frequency interval containing 90% of the signal energy [4].

A. WORST CASE AS MAXIMUM DISSIPATED ENERGY

The following optimization problem defines a worst-case IEMI scenario in which the energy $W_{L,n}$ dissipated in a frequency-dependent impedance $\hat{Z}_{L,n}(\omega)$ connected at the n-th port is maximized, under the constraint of a finite energy-density W_E of the impinging plane-wave field. Specifically, the formulation exploits the frequency domain and the Parseval's theorem to easily express the energy as squared 2-norm of relevant spectrum [29]:

$$\max : W_{L,n} = \frac{1}{2\pi} \int_{-\infty}^{+\infty} \frac{1}{\hat{Z}_{L,n}^*} \left| \hat{V}_{L,n} \right|^2 d\omega$$

$$\text{constraint} : \frac{1}{2\pi Z_0} \int_{-\infty}^{+\infty} \left| \hat{E}_i(\omega) \right|^2 d\omega = W_E \quad (19)$$

By substituting (16) into (19) and accounting for band-limitation and for the conjugate symmetry of spectral

components at negative frequencies, the optimization problem can be reformulated with unilateral spectra as

$$\max : W_{L,n} = \frac{1}{\pi} \int_{\omega_1}^{\omega_2} \text{Re}\left(\hat{Z}_{L,n}^{-1}\right) \left| \hat{E}_i \right|^2 \left| \hat{L}_n \right|^2 d\omega$$

$$\text{constraint} : \frac{1}{\pi Z_0} \int_{\omega_1}^{\omega_2} \left| \hat{E}_i(\omega) \right|^2 d\omega = W_E \quad (20)$$

where Re(...) denotes the real part of a complex variable.

For the analytical solution of (20), it is straightforward to derive an upper bound to the objective function, which inherently includes the constraint:

$$W_{L,n} \leq \frac{1}{\pi} \int_{\omega_1}^{\omega_2} \left| \hat{E}_i \right|^2 \sup_{\omega}\left\{ \text{Re}\left(\hat{Z}_{L,n}^{-1}\right) \left| \hat{L}_n \right|^2 \right\} d\omega$$

$$= \sup_{\omega}\left\{ \text{Re}\left(\hat{Z}_{L,n}^{-1}\right) \left| \hat{L}_n \right|^2 \right\} \frac{1}{\pi} \int_{\omega_1}^{\omega_2} \left| \hat{E}_i \right|^2 d\omega$$

$$= Z_0 W_E \sup_{\omega}\left\{ \text{Re}\left(\hat{Z}_{L,n}^{-1}\right) \left| \hat{L}_n \right|^2 \right\} \quad (21)$$

where the operator $\sup_{\omega}\{.\}$ is intended as the greatest value over the bandwidth. The equal sign in (21) occurs exactly when the energy of the incident electric field is concentrated in a narrow band, centered around a frequency which maximizes the amplitude response of $\text{Re}\left(\hat{Z}_{L,n}^{-1}\right) \left| \hat{L}_n \right|^2$. In other terms, equation (21) states that the worst-case IEMI scenario for the dissipated energy is a narrowband HPEM pulse tuned into the (possibly resonant) frequency for which the electric port exhibits best coupling.

As previously mentioned, sinusoidal steady-state (i.e., zero bandwidth $\omega_2 - \omega_1 = 0$) is not allowed by the proposed analysis, therefore the HPEM signal must always get a certain band-ratio $\omega_2/\omega_1 > 1$. In this connection, Section IV will exemplify that the energy bound represents a converging limit for $\omega_2/\omega_1 \to 1^+$ and that a bandratio as low as 1.01 is enough to approach this limit in practical terms.

As a final comment, it is worth discussing the special case of a resistive, frequency-independent load impedance $\hat{Z}_{L,n} = R_L$. In this condition, the energy W_L in (21) becomes simply proportional to the squared 2-norm of the voltage, and the worst-case bound (12) reduces to

$$W_{L,n} \leq \frac{Z_0 W_E}{R_L} \left(\sup_{\omega}\left\{ \left| \hat{L}_n \right| \right\} \right)^2 \quad (22)$$

which means that the worst-case narrowband signal excites the maximum peak in the amplitude response of the coupling length.

B. WORST CASE AS MAXIMUM VOLTAGE PEAK

The worst-case IEMI scenario for the peak value of the induced voltage (∞-norm) was deeply investigated for one-port systems in a previous work [15], [17], [18], therefore only the main points of the derivation are here reported with emphasis on the multiport formulation.

Let $t = t_0$ be an arbitrary time instant when the voltage induced in the n-th port (18) reaches the peak

$V_{LP,n} = \sup_t \{V_{L,n}(t)\} = V_{L,n}(t_0)$. Aim of the following optimization problem is finding the HPEM pulse which maximizes $V_{LP,n}$ under the finite-energy constraint for the incident field:

$$\max : V_{LP,n} = \frac{1}{2\pi} \int_{-\infty}^{+\infty} \hat{E}_i(\omega) \hat{L}_n(\omega) e^{j\omega t_0} d\omega$$
$$\text{constraint} : \frac{1}{2\pi Z_0} \int_{-\infty}^{+\infty} \left| \hat{E}_i(\omega) \right|^2 d\omega = W_E \quad (23)$$

By accounting for band limitation and for the conjugate symmetry of spectral components at negative frequencies, the optimization problem can be reformulated with unilateral spectra as

$$\max : V_{LP,n} = \frac{1}{\pi} \int_{\omega_1}^{\omega_2} \hat{E}_i(\omega) \hat{L}_n(\omega) e^{j\omega t_0} d\omega$$
$$\text{constraint} : \frac{1}{\pi Z_0} \int_{\omega_1}^{\omega_2} \left| \hat{E}_i(\omega) \right|^2 d\omega = W_E \quad (24)$$

As shown in [15], the Lagrange multiplier method can be used to solve (24) and obtain the spectral density of the worst-case electric field in the form

$$\hat{E}_i(\omega) = \sqrt{\frac{Z_0 \pi W_E}{\int_{\omega_1}^{\omega_2} \left| \hat{L}_n(\omega) \right|^2 d\omega}} \hat{L}_n(\omega)^* e^{-j\omega t_0} \quad (25)$$

and the worst-case peak voltage as

$$V_{LP,n} = \sqrt{\frac{Z_0 W_E}{\pi} \int_{\omega_1}^{\omega_2} \left| \hat{L}_n(\omega) \right|^2 d\omega} \quad (26)$$

The incident electric field given by (25) has a wideband spectrum realizing a sort of energetic matching with the coupling length of the system. Indeed, the energy density W_E of the incident field is distributed in the whole available bandwidth $[\omega_1, \omega_2]$ so that (a) the field magnitude is proportional to the amplitude response of $\hat{L}_n(\omega)$, thus favoring frequencies characterized by good receiving properties; (b) the field phase is the complex conjugate of the phase response of $\hat{L}_n(\omega)$, plus an additional phase shift $-\omega t_0$ which simply enforces peak occurrence at time t_0. Note that t_0 is inconsequential in the expression (26) of the worst-case peak.

Finally, it is worth stressing the contrast between the previous worst-case energy optimization (requiring a narrowband and tuned HPEM field) and this worst-case peak optimization (requiring a wideband HPEM field). For the latter, any narrowband signal with band-ratio $\omega_2/\omega_1 \to 1^+$ would lead to a voltage peak tending to zero, owing to the equal extremes of the integral involved in (26).

C. WORST CASE AS MAXIMUM RECTIFIED IMPULSE
The last worst-case scenario of interest deals with the maximization of rectified impulse $J_{L,n}$ (1-norm) of the induced voltage waveform at the n-th port, under the usual finite-energy constraint for the field. In principle, the problem could

be stated as

$$\max : J_{L,n} = \int_{-\infty}^{+\infty} \left| V_{L,n}(t) \right| dt$$
$$\text{constraint} : \frac{1}{2\pi Z_0} \int_{-\infty}^{+\infty} \left| \hat{E}_i(\omega) \right|^2 d\omega = W_E \quad (27)$$

However, such an optimization turns out to be ill-posed since $J_{L,n}$ is not actually bounded. This property can be rigorously demonstrated by resorting to Hölder's inequality for p norms [24]

$$\|s_1 s_2\|_1 \leq \|s_1\|_p \|s_2\|_q; \quad p^{-1} + q^{-1} = 1 \quad (28)$$

By assuming $s_1 = s_2 = V_{L,n}(t)$, $p = 1$, $q \to \infty$ in (28), the following lower bound is readily derived

$$J_{L,n} \geq \frac{\left\| V_{L,n}(t) \right\|_2^2}{\left\| V_{L,n}(t) \right\|_\infty} = \frac{\left\| V_{L,n}(t) \right\|_2^2}{V_{LP,n}} \quad (29)$$

Therefore, the rectified-impulse is no less than the ratio between the squared 2-norm and the ∞-norm (i.e., peak) of the induced voltage. According to the final observation in Section III.B, denominator $V_{LP,n}$ of (29) tends to zero in case of narrowband excitation. Conversely, the squared 2-norm in the numerator of (29) converges to a non-null value (as it can be demonstrated by exploiting results of Section III.A). As a result, any narrowband signal with band-ratio $\omega_2/\omega_1 \to 1^+$ leads to $J_{L,n} \to \infty$ regardless of frequency. Consequently, the rectified impulse can be made arbitrarily great by reducing the bandwidth. Moreover, if the center frequency of the narrowband signal was optimally tuned according to Section III.A, a worst-case condition for energy would be simultaneously reached.

To provide physical insight, one can observe that the narrower is the band of a finite-energy signal, the longer is its duration in time. Hence, concerning the IEMI stress level associated with the rectified impulse, the key role is actually played by signal duration.

IV. APPLICATION EXAMPLE
A case study is proposed to exemplify and corroborate the worst-case IEMI assessment method. After a brief introduction to the multiport system of interest (LVDS interconnect), the case study develops in three parts. First, the reciprocity-based approach to field coupling presented in Section II is validated. Second, three worst-case IEMI scenarios theoretically discussed in Section III are demonstrated by numerical simulation. The last part takes advantage of computational efficiency to carry out a statistical analysis based on repeated-run simulations, aimed at accounting for lack of knowledge about the direction of arrival and polarization of the HPEM field, as well as uncertainty of system parameters.

A. LVDS INTERCONNECT
The victim system under analysis is a LVDS driver-receiver interconnect. Owing to several advantages like low energy consumption, high CM noise rejection and easy integration
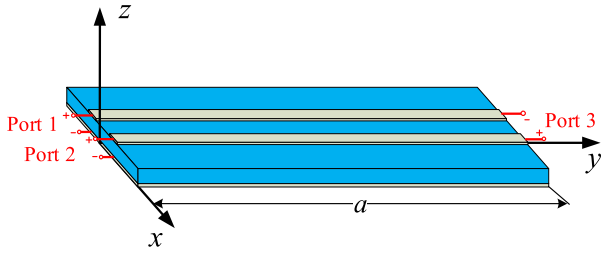
FIGURE 5. Architecture of a microstrip DL for LVDS. The PCB lies in the x-y plane. Two ports are defined at the left end (driver terminal) and a differential port is defined at the right end (receiver terminal).
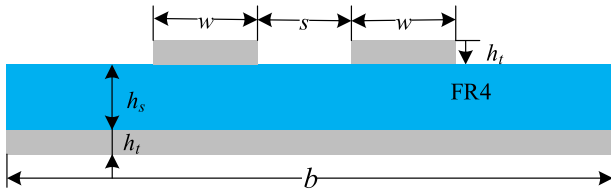

FIGURE 6. Transverse cross section of the PCB in Fig. 5.

FIGURE 7. Terminal loading conditions for the LVDS interconnect in Fig. 5.

FIGURE 8. Magnitude of the complex radiation pattern (10) of the LVDS interconnect in Fig. 5 at the frequency of 6 GHz, when port 3 is connected to a voltage source with series impedance 50 Ω, and delivers 1 W forward power, while port 1 and port 2 are terminated with 50 Ω impedances.

in PCB, the LVDS standard is nowadays widely adopted for high-speed differential data transmission [30]. A typical LVDS system is composed of three parts, namely: a driver circuit for digital signal generation, a differential line (DL) for signal transmission, and a receiver for signal reception. Since the nominal LVDS operating voltage level is quite low (typically 0.35 V), the susceptibility to externally induced interference (like radiated IEMI) is more critical than for other transmission standards.

As shown in Fig. 5, a canonical architecture of DL for LVDS consists in parallel PCB microstrip lines of length a and width b. Three electrical ports are defined: port 1 and port 2 are single-ended ports referenced to the ground plane at the driver's terminal, while port 3 is a differential port at the receiver's terminal.

The cross section is depicted in Fig. 6. The dielectric layer of the PCB is a Flame-Retardant 4 laminate (FR4, relative permittivity $\varepsilon_{r,FR4} = 4.3$, dielectric-loss angle tangent $\tan \delta_{FR4} = 0.02$). Microstrips and ground layer are made of copper with conductivity $\sigma_{Cu} = 5.96 \times 10^7$ S/m. Geometrical parameters defined in Fig. 5 and Fig. 6 are: $a = 50$ mm; $b = 10$ mm; $h_s = 0.22$ mm; $w = 0.3$ mm; $s = 0.36$ mm; $h_t = 50\ \mu$m.

For the transverse-electromagnetic transmission-line mode of propagation [30], [31], the CM and the differential-mode (DM) characteristic impedances can be estimated through approximate formulas

$$Z_{CM} \approx \frac{60}{\sqrt{0.457\varepsilon_r + 0.67}} \ln\left(\frac{4h_s}{0.67(0.8w + h_t)}\right) = 55.8\ \Omega \tag{30}$$

$$Z_{DM} \approx 2Z_0\left(1 - 0.48e^{-0.95\frac{s}{h_s}}\right) = 100.3\ \Omega \tag{31}$$

Though driver and receivers are essentially non-linear devices as far as the functional operation is concerned [32],
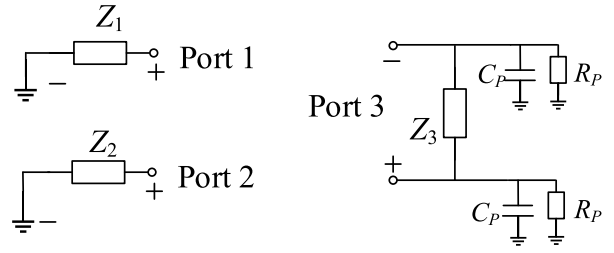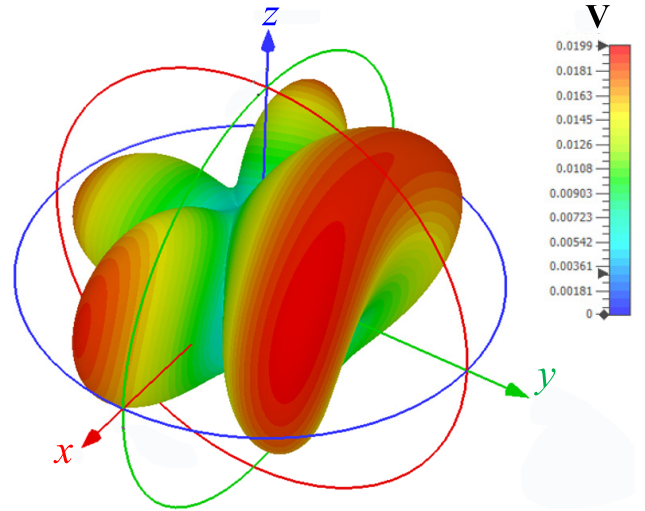
their terminal behavior at very-high and microwave frequencies can be modelled by the linear equivalent circuits shown in Fig. 7, of large use in electromagnetic compatibility analysis. At the balanced driver's terminal, line-to-ground impedances are $Z_1 = Z_2 = 50\ \Omega$. At the receiver's terminal, impedance $Z_3 = 100\ \Omega \approx Z_{DM}$ ensures DM matching, while the parasitic capacitors $C_P = 2$ nF and resistors $R_P = 160$ kΩ account for non-ideal floating conditions [30], [31].

B. RECIPROCITY-BASED COUPLING LENGTH

For the solution of the transmitting-mode problem in Section II.A, the Finite Integration Technique (FIT) implemented in the commercial software [33] was used. The bandwidth of interest $[f_1, f_2] = [0.3,\ 6]$ GHz was purposely selected to cover the typical frequency range of ultra-wideband (UWB) radiated-IEMI disruptors [4]. The full-wave simulations took about 50 min on a personal computer (16 GB RAM, clock 3.4 GHz). An example of radiation pattern is shown in Fig. 8. For processing and storing the output quantities of interest (i.e., input impedance $\hat{\mathbf{Z}}_a$ and radiation pattern $\vec{\hat{\mathbf{F}}}$), the frequency range was linearly sampled with step $\Delta f = 50$ MHz, and the angular coordinates θ and ϕ were linearly sampled with step of $2°$. Standard
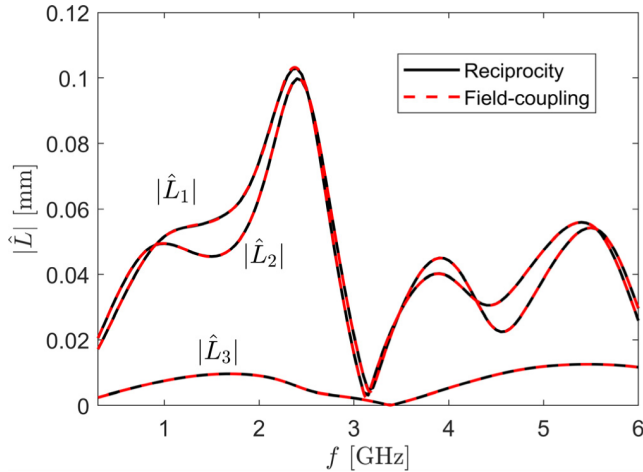
FIGURE 9. Comparison of the coupling lengths (magnitude) for the three ports defined in Fig. 5, evaluated by the proposed reciprocity-based approach and by direct field-coupling simulations.

FIGURE 10. Spectral density (magnitude) of different HPEM fields introduced in Sec. IV.C.

interpolation techniques can be applied to such a data set to retrieve intermediate samples.

By post-processing of these data, one can now exemplify and validate the calculation of the coupling length $\hat{\mathbf{L}}$ defined in Section II.B. Without loss of generality, an impinging plane-wave field with incidence angles $\theta = 73°; \phi = 0$ and polarization angle $\eta = 45°$ is assumed. The amplitude responses of the three coupling lengths (one for each electric port) obtained from the application of reciprocity according to (17) are plotted with solid lines in Fig. 9.

The FIT numerical solver [33] was used to carry out an independent simulation by illuminating the system with the specific plane-wave field defined above and by directly solving the field-coupling problem. The coupling lengths so obtained are plotted with dashed lines in Fig. 9 and result in very good agreement with those evaluated by reciprocity, thus validating the proposed approach. It is worth stressing again that the advantage of the proposed approach resides in the limited computational burden. Indeed, while the direct FIT simulation of field-coupling (valid just for a specific plane-wave incidence and polarization) takes 40 minutes, the post-processing of input-impedance and radiation pattern to get the reciprocity-based coupling length takes less than 10 seconds and could be carried out for any possible incidence and polarization angle.

From Fig. 9, one may also notice that the coupling length of port 3 is much lower than those of port 1 and port 2, which proves the excellent (though not perfect) noise immunity of DM in a balanced DL.

C. WORST-CASE IEMI ASSESSMENT

Once the coupling length is found, the three IEMI worst-case scenarios (dissipated energy, voltage peak, rectified impulse) can be addressed. For the sake of brevity, only results for port 3 are here reported, considering that this differential port plays a crucial role for susceptibility effects since it carries the LVDS digital signal.
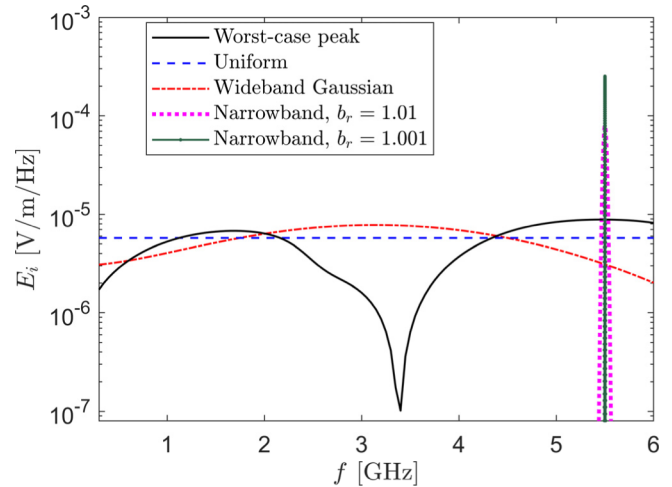
The HPEM field is assumed to have a typical energy density $W_E = 1$ mJ/m^2 [12]. To validate the worst-case conditions theoretically derived in Section III, five different waveforms (all having the same W_E) are defined, and their spectral densities (magnitude) are plotted in Fig. 10.

The first waveform is the worst-case wideband signal (25) maximizing the voltage peak. As expected, the magnitude of its spectrum is a scaled version of the coupling length $|\hat{L}_3|$. The time-domain waveform can be obtained through IFT.

The fourth and fifth signal in Fig. 10 are narrowband and apt to reach the worst-case condition for the dissipated energy in (21). In particular, these waveforms are Gaussian-modulated sinusoids in the form [4]

$$E_i(t) = A \cos[2\pi f_c(t - t_d)]e^{-\frac{(t-t_d)^2}{\tau^2}} \quad (32)$$

where variable A scales the amplitude of the electric field, $t_d \approx 4.47\tau_0$ translates the waveform along the time axes, $\tau = 0.74/(f_2 - f_1)$ assures 90% of the energy falls into the frequency band $[f_1, f_2]$ and $f_c = (f_1 + f_2)/2$ is the center frequency, tuned at $f_c = 5.47$ GHz, that is, in the maximum of coupling length $|\hat{L}_3|$. The two narrowband signals differ for the band-ratio $b_r = f_2/f_1$, set to $b_r = 1.01$ and $b_r = 1.001$, respectively.

The remaining two electric-field spectra in Fig. 10 pertain to canonical wideband waveforms usually considered for modeling HPEM environments and significant to our exemplification purposes [4]. One presents a uniformly distributed spectrum (and constant phase) in the bandwidth of interest, and the other one is a hyperband Gaussian waveform like (32) with a very large bandratio $b_r = f_2/f_1 = 6/0.3 = 20$.

In Fig. 11, the three wideband waveforms (worst-case peak, uniform and wideband-Gaussian) are reported in a short time widow (8-13 ns) for optimal readability. The narrowband waveforms are omitted not only because their plot would require different axis scaling, but also because their
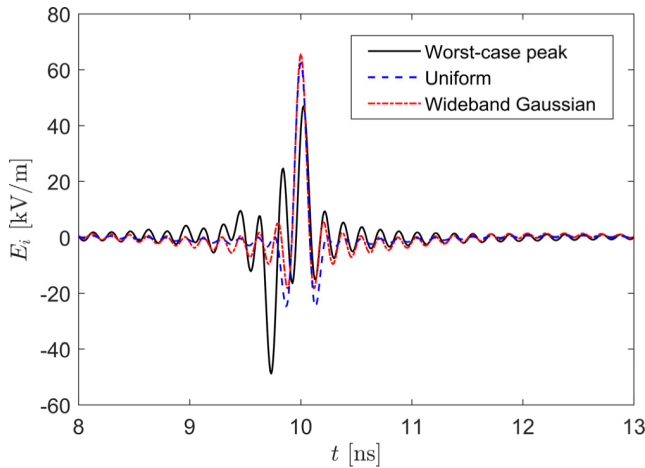
FIGURE 11. Electric-field waveforms of three wideband HPEM pulses defined in Sec. IV.C and corresponding to spectral densities shown in Fig. 10.
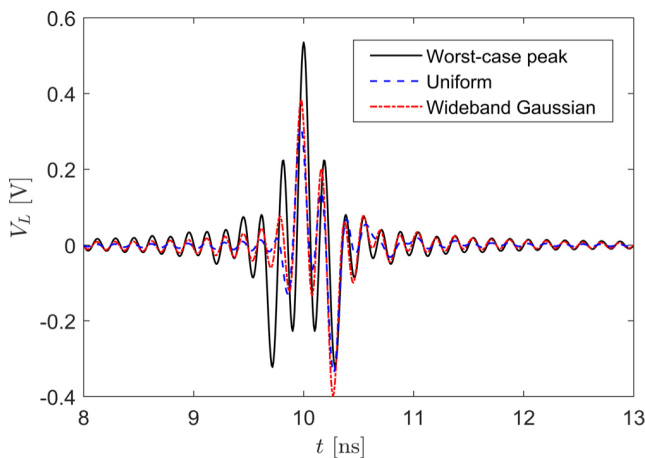

FIGURE 12. Voltage waveforms induced at port 3 of the LVDS interconnect by the wideband HPEM fields shown in Fig.11.

slowly modulated single-tone behavior results to be obvious from (32).

The voltage waveforms induced at port 3 evaluated by (18) are plotted in Fig. 12 (three wideband cases) and Fig. 13 (two narrowband cases). The figures of merit for susceptibility effects estimated by their definition (peak, dissipated energy, rectified impulse) are summarized in Table 2.

The obtained results can be discussed to offer a solid numerical proof to the optimality of the investigated worst-case scenarios. First, one can clearly appreciate that the "worst-case peak" signal in Fig. 12 actually reaches the largest voltage peak V_{LP} among all the waveforms, as expected from the theoretical framework developed in Section III.B. In particular, it is interesting that the peak value is lower for the uniform and the wideband-gaussian cases, despite their impinging HPEM waves show greater electric-field peaks in Fig. 11. The peaks reached by narrowband waveforms in Fig. 13 are much lower than the worst-case one, despite the center frequency is tuned in a maximum
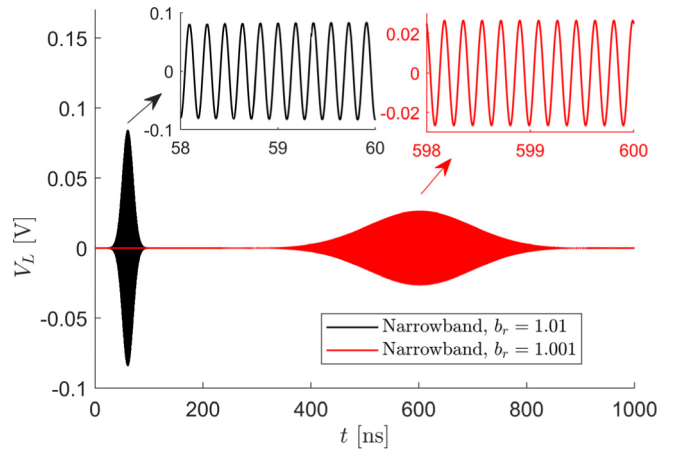

FIGURE 13. Voltage waveforms induced at port 3 of the LVDS interconnect by the narrowband HPEM fields whose spectrum is shown in Fig.10. Insets show details in short-time windows.

TABLE 2. Figures of merit.

HPEM field	V_{LP} [V]	W_L [J]	J_L [V·s]
Worst-case peak	0.535	4.07×10^{-13}	2.56×10^{-10}
Uniform	0.398	2.50×10^{-13}	1.82×10^{-10}
Wideband Gaussian	0.337	1.72×10^{-13}	1.18×10^{-10}
Narrowband, b_r=1.01	0.084	5.97×10^{-13}	1.28×10^{-9}
Narrowband, b_r=1.001	0.027	5.97×10^{-13}	4.04×10^{-9}

of the coupling length. Moreover, their peak decreases if the band-ratio is reduced, as observed in the end of Section III.B.

Concerning the dissipated energy W_L, its greatest value is achieved by the tuned narrowband waveforms in Fig. 13, with no appreciable difference with respect to bandratios. This result agrees with theoretical derivations presented in Section III.A and shows, specifically, that even a bandratio b_r =1.01 (relatively large for a narrowband waveform) is sufficient to reach the energy limit predicted in (21).

Finally, the rectified-impulse J_L is significantly larger for narrowband than for wideband waveforms, as expected from Section III.C. Moreover, J_L is more than three times larger when the bandratio decreases from 1.01 to 1.001, in accordance with the increased duration of signal.

D. STATISTICAL ANALYSIS
The worst-case voltage peak and energy and the unbounded rectified impulse can be used as effective figures of merit in IEMI risk assessment, since they summarize a complex waveform through significant norms well correlated to susceptibility/damage effects. It should be noted, however, that these parameters strictly depend on the incidence angles θ, ϕ and the polarization angle η of the incident plane-wave field, which are hardly foreseeable in any realistic IEMI attack (for instance, all results in Table 2 refer just to specific values mentioned in Section IV.B). Moreover, geometrical or electrical parameters of the system may be affected by uncertainty
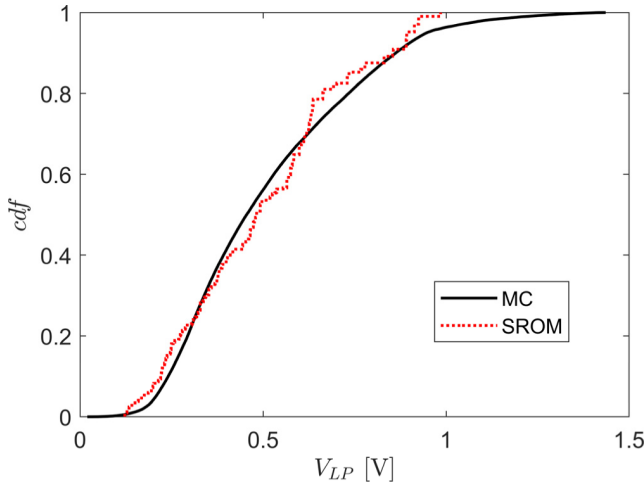
FIGURE 14. Cdf of the worst-case voltage peak for random incidence and polarization angles.

FIGURE 15. Cdf of the worst-case dissipated energy for random incidence and polarization angles.

as well. It is therefore essential to introduce a statistical representation of relevant input parameters as RVs and carry out the evaluation of the worst-case figures of merit via uncertainty-quantification methods.

The computational burden is quite different depending on the role played by RVs in the reciprocity-based computational method. Specifically, accounting for variations of the wave angles θ, ϕ, η and load impedances connected at the ports is relatively inexpensive, since it does not require to re-evaluate the radiation pattern and the input impedance matrix. Hence, a computationally-efficient MC method can leverage repeated post-processing of $\vec{\bar{\mathbf{F}}}$, $\hat{\mathbf{Z}}_{\mathbf{a}}$ while no further full-wave simulations are required. Conversely, variations of internal geometric/electrical parameters of the victim system impact on the radiation pattern and input impedance, therefore it becomes compulsory repeating time-consuming full-wave simulations for each sample point in the RV space. Consequently, the conventional MC method requiring thousands of repeated runs would be no longer an option. As a trade-off between computational time and quality of the statistical characterization, a SROM method is here proposed to predict statistical estimates (i.e., mean and standard deviation) and cdf using few RV samples [14], [34].

Once again, the LVDS system in Section III.A is used for exemplification. The HPEM field has energy density $W_E = 1$ mJ/m^2 in the bandwidth 300 MHz − 6 GHz, with fully unknown direction of incidence and polarization, which are modeled through independent uniformly (U) distributed RVs

$$\theta \sim \mathrm{U}\left[0°, 180°\right]$$
$$\phi \sim \mathrm{U}\left[0°, 360°\right]$$
$$\eta \sim \mathrm{U}\left[0°, 360°\right] \tag{33}$$

The empirical cdfs of the worst-case voltage peak V_{LP} and dissipated energy W_L predicted by MC and SROM are plotted in Fig. 14 and Fig. 15, respectively. The MC method was based on 10^5 randomly generated samples (each one
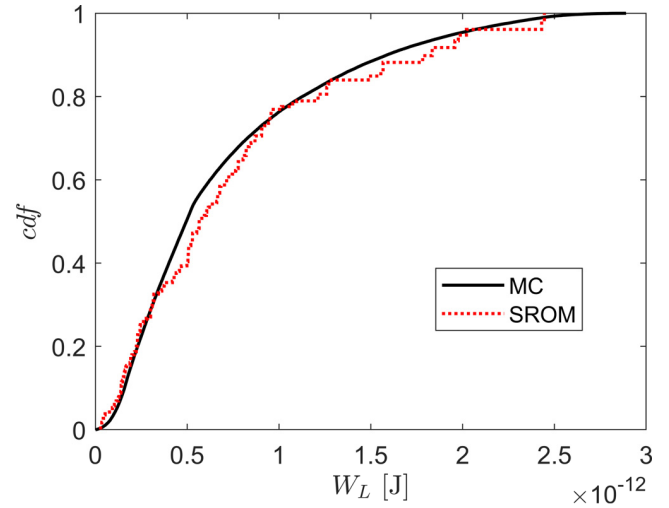
**TABLE 3.** Comparison of statistics analysis results by MC and SROM, RVs: Incidence and polarization angles.

	Method	V_{LP} [V]	W_L [J]
Time-consumption	MC	$\approx$ 50 min+4 min	
	SROM	$\approx$ 50 min+1 min	
Mean	MC	0.51	6.96×10⁻¹³
	SROM	0.50	7.28×10⁻¹³
Standard deviation	MC	0.25	5.76×10⁻¹³
	SROM	0.23	6.17×10⁻¹³

composed of three values, one for each RV) and the total time cost resulted to be the sum of 50 min, spent in full-wave electromagnetic simulation, plus 4 min devoted to repeated-run post processing. For the SROM method, 5 samples for each variable were selected, leading to 5^3 =125 samples of the RV space, deterministically chosen according to the optimal sampling strategy presented in [34]. Moreover, as a further optimization allowed by geometrical symmetry in Fig. 5, RVs were sampled in $\theta \sim \mathrm{U}\left[0°, 180°\right]$, $\phi \sim \mathrm{U}\left[-90°, 90°\right]$ and $\eta \sim \mathrm{U}\left[0°, 180°\right]$. Such a SROM method resulted to be slightly faster than MC, since post-processing time reduced to less than 1 min.

The cdfs pertaining to MC and SROM (the latter being obviously coarser) are in good agreement in Fig. 14 and Fig. 15. The associated mean and standard deviation are reported in Table 3. Their comparison is significant, since the adopted SROM algorithm is specifically targeted to optimize the accuracy of statistical estimates evaluated with few RV samples [34]. From Table 3, one can appreciate that the relative error of SROM versus MC results is smaller than 8% for the mean and 7% for the standard deviation.

In addition, Fig. 14 and Fig. 15 prove the sensitivity of the worst-case voltage peak and dissipated energy to the variation of wave angles. Indeed, V_{LP} may vary from almost zero to 1.44 V, whereas, the worst-case energy W_L ranges from zero to 2.89 pJ. In general, the obtained cdfs prove that
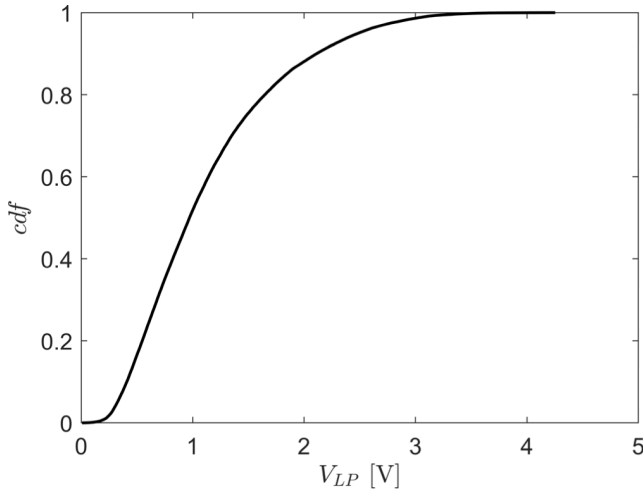
FIGURE 16. Cdf of the worst-case voltage peak for random incidence angles, polarization angle, and trace separation.

FIGURE 17. Cdf of the worst-case dissipated energy for random incidence angles, polarization angle, and trace separation.

susceptibility effects are possible. For instance, the 0.3-quantile of the worst-case voltage peak is about 0.35 V in Fig. 14, that is, equal to the nominal DM voltage of LVDS digital signals [32]. Hence, the probability to induce an even higher peak (implying almost certain malfunction/damage of the LVDS link) is as high as 70%.
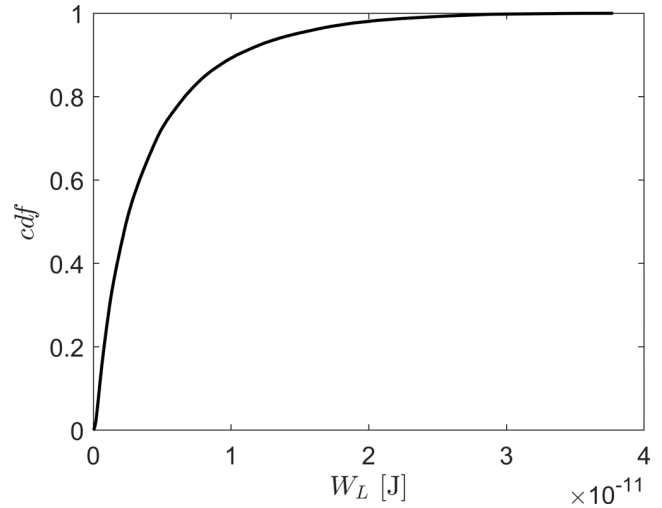
From the computational times discussed above, actually dominated by the full-wave simulation task, the advantage of SROM over MC is not manifest. Nevertheless, SROM results have been reported for demonstration and validation purposes. Actually, the full potential of SROM can be really appreciated for the treatment of specific RVs, like geometrical parameters, having an impact on the radiation pattern and input impedance. To exemplify this concept, another statistical analysis is presented in the following.

Let us consider unknown direction of incidence and polarization described by uniformly distributed RVs (33) and, in addition, uncertainty of the trace separation s shown in Fig. 6, which is modeled as a RV with distribution

$$s \sim \text{U} [0.36 \text{ mm}, 1.8 \text{ mm}] \tag{34}$$

A combined MC/SROM method is proposed to solve this mixed uncertainty-quantification problem. Six samples of s were optimally selected by resorting to the SROM algorithm [34]. Consequently, a feasible number of six full-wave simulations were performed, to re-evaluate the radiation pattern and input impedance. Conversely, computationally inexpensive wave angles were treated by the accurate MC approach. Results of post-processing can be combined so to generate the empirical cdfs in Fig. 16 and Fig. 17 and the statistical estimates in Table 4. In contrast to the stepped cdfs predicted by pure SROM in previous figures, cdfs in Figs. 16-17 are smooth since the combined SROM/MC method exploits a total number of 10^5 random samples.

In terms of computational time, the statistical analysis costs 300 min to complete six full-wave simulations of 50 min

TABLE 4. Statistical analysis results by combined MC/SROM, RVs: Wave angles and trace separation.

	V_{LP}[V]	W_L[J]
Time-consumption	$\approx$ 6×50 min+6 min	
Mean	1.13	4.21×10^{-12}
Standard deviation	0.67	4.88×10^{-12}

plus about 6 min for post-processing. Hence, the total time remains within reasonable feasibility limits.

It is worth noting that the predicted mean and standard deviation in Table 4 are much larger (both for voltage peak and for energy) than those in Table 3. This observation proves the importance of the considered geometrical RV. This aspect can be further appreciated in Fig. 16 and Fig. 17, where ranges of cdfs have significantly widened. Namely, the quantile associated to nominal LVDS operation voltage (0.35 V) is reduced to 0.06, while the upper extreme of V_{LP} is tripled (4.3 V) with respect to the upper extreme in Fig. 14. Likewise, the upper extreme of W_L reaches 37.8 pJ in Fig. 17, that is, more than ten times larger than in Fig. 15.

V. CONCLUSION

This paper presented a computational-efficient IEMI assessment method based on full-wave simulation. Field coupling to an N-port victim system is modeled through the Lorentz reciprocity theorem. Namely, a full-wave numerical solver of Maxwell's equations is used to carry out N frequency-domain simulations of the system in transmitting mode, targeted to the evaluation of the N-by-N input impedance matrix and N normalized radiation patterns. Results are stored in memory and subsequently post-processed to evaluate the voltage waveforms induced at the N-ports by an HPEM field for any possible incidence and polarization angles.

The definition of coupling length enabled the statement and closed-form solution of optimization problems defining worst-case IEMI scenarios for three different figures of merit related to susceptibility effects, namely, the dissipated energy, the peak and the rectified impulse of the induced voltage. Constrains of this optimization problems were the limited bandwidth and the finite energy density of the HPEM field. It was analytically demonstrated that worst-case dissipated energy can be achieved when the system is excited by a narrowband HPEM pulse, whose center frequency is tuned in the maximum of the amplitude response of the coupling length. Conversely, the worst-case voltage peak can be achieved for a wideband HPEM waveform, whose spectrum density is properly matched to the whole frequency response of the coupling length according to (25). The rectified pulse turned out to be unbounded and could be made arbitrarily great by reducing the bandwidth of any narrowband HPEM pulse.

A PCB interconnect for LVDS was analyzed to exemplify various outputs of the proposed IEMI assessment method, as well as to validate the worst-case scenarios. Eventually, statistics was introduced to account for lack of knowledge and uncertainty about electrical and geometrical parameters of the system. It was shown that a conventional MC method can be efficiently used to characterize the cdf of the worst-case voltage peak and dissipated energy resulting for random incidence/polarization angles and random terminal loads. Indeed, repeated-run simulations are just based on post-processing of the same reciprocity-based parameters. Conversely, the introduction of RVs related to internal system properties like geometrical parameters demands for the re-evaluation of the input impedance matrix and radiation patterns through several full-wave simulations, which is prohibitive in terms of computational burden. In this case, the application of SROM in combination with MC proved to be effective to maintain the number of repeated runs and the associated computational time within reasonable limits.

REFERENCES

[1] W. A. Radasky, "Protection of commercial installations from the high-frequency electromagnetic threats of HEMP and IEMI using IEC standards," in *Proc. Asia–Pacific Int. Symp. Electromagn. Compat.*, Apr. 2010, pp. 758–761.

[2] F. Sabath, "What can be learned from documented Intentional Electromagnetic Interference (IEMI) attacks?" in *Proc. 30th URSI Gen. Assem. Sci. Symp.*, Aug. 2011, pp. 1–4.

[3] W. A. Radasky, "Fear of frying electromagnetic weapons threaten our data networks. Here's how to stop them," *IEEE Spectrum*, vol. 51, no. 9, pp. 46–51, Sep. 2014.

[4] *Electromagnetic Compatibility (EMC)—Part 2-13: Environment—High-Power Electromagnetic (HPEM) Environments—Radiated and Conducted*, Standard IEC 61000, 2005.

[5] W. A. Radasky, C. E. Baum, and M. W. Wik, "Introduction to the special issue on high-power electromagnetics (HPEM) and intentional electromagnetic interference (IEMI)," *IEEE Trans. Electromagn. Compat.*, vol. 46, no. 3, pp. 314–321, Aug. 2004.

[6] D. V. Giri and F. M. Tesche, "Classification of intentional electromagnetic environments (IEME)," *IEEE Trans. Electromagn. Compat.*, vol. 46, no. 3, pp. 322–328, Aug. 2004.

[7] C. E. Baum, E. G. Farr, and D. V. Giri, "Review of impulse-radiating antennas," in *Review of Radio Science 1996-1999*. Hoboken, NJ, USA: Wiley, 1999, pp. 403–439.

[8] M. Ianoz, B. I. C. Nicoara, and W. A. Radasky, "Modeling of an EMP conducted environment," *IEEE Trans. Electromagn. Compat.*, vol. 38, no. 3, pp. 400–413, Aug. 1996.

[9] N. Mora, I. D. Flintoft, L. Dawson, J. F. Dawson, F. Rachidi, M. Rubinstein, A. C. Marvin, P. Bertholet, and M. Nyffeler, "Experimental characterization of the response of an electrical and communication raceway to IEMI," *IEEE Trans. Electromagn. Compat.*, vol. 58, no. 2, pp. 494–505, Apr. 2016.

[10] F. Brauer, F. Sabath, and J. L. T. Haseborg, "Susceptibility of IT network systems to interferences by HPEM," in *Proc. IEEE Int. Symp. Electromagn. Compat.*, Aug. 2009, pp. 237–242.

[11] F. Sonnemann and J. Mirschberger, "Susceptibility of a generic CAN-bus network against high-power electromagnetics (HPEM)," in *Proc. Int. Conf. Electromagn. Adv. Appl.*, Sep. 2009, pp. 174–177.

[12] D. Nitsch, M. Camp, F. Sabath, J. L. T. Haseborg, and H. Garbe, "Susceptibility of some electronic equipment to HPEM threats," *IEEE Trans. Electromagn. Compat.*, vol. 46, no. 3, pp. 380–389, Aug. 2004.

[13] K.-J. Li, Y.-Z. Xie, Y.-H. Chen, and Y.-C. Hui, "Multinomial regression model for the evaluation of multilevel effects caused by high-power electromagnetic environments," *IEEE Trans. Electromagn. Compat.*, vol. 61, no. 1, pp. 149–156, Feb. 2019.

[14] Z. Fei, Y. Huang, J. Zhou, and C. Song, "Numerical analysis of a transmission line illuminated by a random plane-wave field using stochastic reduced order models," *IEEE Access*, vol. 5, pp. 8741–8751, 2017.

[15] G. Spadacini, T. Liang, F. Grassi, and S. A. Pignari, "Worst case and statistics of waveforms involved in wideband intentional electromagnetic attacks," *IEEE Trans. Electromagn. Compat.*, vol. 60, no. 5, pp. 1436–1444, Oct. 2018.

[16] G. Andrieu, L. KonÉ, F. Bocquet, B. DÉmoulin, and J.-P. Parmantier, "Multiconductor reduction technique for modeling common-mode currents on cable bundles at high frequency for automotive applications," *IEEE Trans. Electromagn. Compat.*, vol. 50, no. 1, pp. 175–184, Feb. 2008.

[17] T. Liang, G. Spadacini, F. Grassi, and S. A. Pignari, "Coupling of wideband radiated IEMI to wiring harness: A statistical analysis of the main influencing parameters," in *Proc. IEEE Symp. Electromagn. Compat., Signal Integrity Power Integrity*, Jul./Aug. 2018, pp. 357–362.

[18] T. Liang, G. Spadacini, F. Grassi, and S. A. Pignari, "Coupling of wideband radiated IEMI to cables above ground," *IEEE Trans. Electromagn. Compat.*, to be published. doi: 10.1109/temc.2018.2877508.

[19] T. Liang, G. Spadacini, F. Grassi, and S. A. Pignari, "Radiated wideband IEMI: Coupling model and worst-case analysis for smart grid wiring harness," in *Proc. IEEE Int. Conf. Environ. Elect. Eng., IEEE Ind. Commercial Power Syst. Eur. (EEEIC / I,CPS Europe)*, Jun. 2018, pp. 1–6.

[20] T. Liang, G. Spadacini, F. Grassi, and S. A. Pignari, "Worst-case wideband radiated IEMI for unshielded and shielded cables: A statistical analysis of the main influencing parameters," *IEEE Trans. Electromagn. Compat.*, to be published. doi: 10.1109/temc.2019.2909824.

[21] D. V. Giri, *High-Power Electromagnetic Radiators: Nonlethal Weapons and Other Applications (The Electromagnetics Library)*. Cambridge, MA, USA: Harvard Univ. Press, 2004.

[22] J. P. Castillo and L. Marin, *Measurements of System Responses to Transient Excitations*. New York, NY, USA: Van Nostrand Reinhold Company, 1986.

[23] W. L. Vault, "The damage susceptibility of integrated circuits to a simulated IEMP transient," *IEEE Trans. Nucl. Sci.*, vol. NS-20, no. 6, pp. 40–47, Dec. 1973.

[24] C. E. Baum. (Mar. 17, 2001). *Relationships Between Time-and Frequency-Domain Norms of Scalar Functions Mathematic Notes*. [Online]. Available: http://ece-research.unm.edu/summa/notes/

[25] J. J. Pantoja, N. Peña, N. Mora, F. Rachidi, F. Vega, and F. Román, "On the electromagnetic susceptibility of hot wire-based electroexplosive devices to RF sources," *IEEE Trans. Electromagn. Compat.*, vol. 55, no. 4, pp. 754–763, Aug. 2013.

[26] D. M. Pozar, *Microwave Engineering*. Hoboken, NJ, USA: Wiley, 2009.

[27] C. A. Balanis, *Antenna Theory: Analysis and Design*. Hoboken, NJ, USA: Wiley, 2005.

[28] M. Stumpf, *Electromagnetic Reciprocity in Antenna Theory*. Hoboken, NJ, USA: Wiley, 2017.

[29] D. M. Pozar, "Waveform optimizations for ultrawideband radio systems," *IEEE Trans. Antennas Propag.*, vol. 51, no. 9, pp. 2335–2345, Sep. 2003.

[30] LVDS Owner's Manual, *Low Voltage Differential Signaling*, 3rd ed. Santa Clara, CA, USA: National Semiconductor Corporation, 2004.

[31] *IEEE Standard for Low-Voltage Differential Signals (LVDS) for Scalable Coherent Interface (SCI)*, IEEE Standard 1596.31996.

[32] A. Boni, A. Pierazzi, and D. Vecchi, "LVDS I/O interface for Gb/s-per-pin operation in 0.35-μm CMOS," *IEEE J. Solid-State Circuits*, vol. 36, no. 4, pp. 706–711, Apr. 2001.

[33] CST Microwave Studio. (2018). *User Manuals*. [Online]. Available: http://www.cst.com

[34] T. Liang, F. Grassi, G. Spadacini, and S. A. Pignari, "Statistical estimation of crosstalk through a modified stochastic reduced order model approach," *IEICE Trans. Commun.*, vol. E101.B, no. 4, pp. 1085–1093, Apr. 2018.

TAO LIANG received the B.Sc. degree in electrical engineering from Xi'an Jiaotong University, Shaanxi, China, in 2013, the M.Sc. degree in electrical engineering from Xi'an Jiaotong University, and the M.Sc. degree *(summa cum laude)* from Politecnico di Milano, Milan, Italy, in 2016. He is currently pursuing the Ph.D. degree in electrical engineering with Politecnico di Milano. His research interests include electromagnetic compatibility modeling and testing techniques.

GIORDANO SPADACINI (M'07–SM'16) received the Laurea (M.Sc.) and Ph.D. degrees in electrical engineering from Politecnico di Milano, Italy, in 2001 and 2005, respectively, where he is currently an Associate Professor with the Department of Electronics, Information and Bioengineering.

His research interests include statistical models for the characterization of interference effects, distributed parameter circuit modeling, experimental procedures and setups for EMC testing, and EMC in aerospace, automotive, and railway systems. He was a recipient of the 2005 EMC Transactions Prize Paper Award, the 2016 Richard B. Schulz Best EMC Transactions Paper Award, and two Best Symposium Paper Award from the 2015 Asia-Pacific International Symposium on EMC (APEMC) and the 2018 Joint IEEE EMC and APEMC Symposium.

FLAVIA GRASSI (M'07–SM'13) received the Laurea (M.Sc.) and Ph.D. degrees in electrical engineering from Politecnico di Milano, Italy, in 2002 and 2006, respectively, where she is currently an Associate Professor with the Department of Electronics, Information and Bioengineering.

From 2008 to 2009, she was with the European Space Agency (ESA), The Netherlands, as a Research Fellow. Her research interests include distributed parameter circuit modeling, statistical techniques, the characterization of measurement setups for EMC testing, and powerline communications. She has received the URSI Young Scientist Award, in 2008, and the IEEE Young Scientist Award from the 2016 Asia-Pacific International Symposium on EMC (APEMC). She was a recipient of the IEEE EMC Society 2016 Transactions Prize Paper Award, and the Best Symposium Paper Award from the 2015 APEMC and the 2018 Joint IEEE EMC and APEMC Symposium.

SERGIO AMEDEO PIGNARI (M'01–SM'07–F'12) received the Laurea (M.Sc.) and Ph.D. degrees in electronic engineering from Politecnico di Torino, Italy, in 1988 and 1993, respectively.

From 1991 to 1998, he was an Assistant Professor with the Department of Electronics, Politecnico di Torino, Turin, Italy. In 1998, he joined Politecnico di Milano, Milan, Italy, where he is currently a Full Professor with the Department of Electronics, Information, and Bioengineering, and Chair of the B.Sc. and M.Sc. degree Programs in electrical engineering. His research interests include the field of EMC and field-to-wire coupling and crosstalk, conducts immunity and emissions in multi-wire structures, statistical techniques for EMC, and experimental procedures and setups for EMC testing. His research activities are mainly related to aerospace, automotive, energy, and railway industry sectors.

Dr. Pignari has been a Member of the Technical Program Committee of the Asia Pacific EMC Week, since 2010. He was a recipient of the 2005 and 2016 IEEE EMC Society Transactions Prize Paper Award, and the 2011 IEEE EMC Society Technical Achievement Award. From 2010 to 2015, he was the IEEE EMC Society Chapter Coordinator. He was the Technical Program Chair of the ESA Workshop on Aerospace EMC, in 2009, 2012, 2016, 2019. He is currently serving as an Associate Editor of the IEEE TRANSACTIONS ON EMC.

• • •